Plasma Sources
Science and
Technology

PAPER • **OPEN ACCESS**

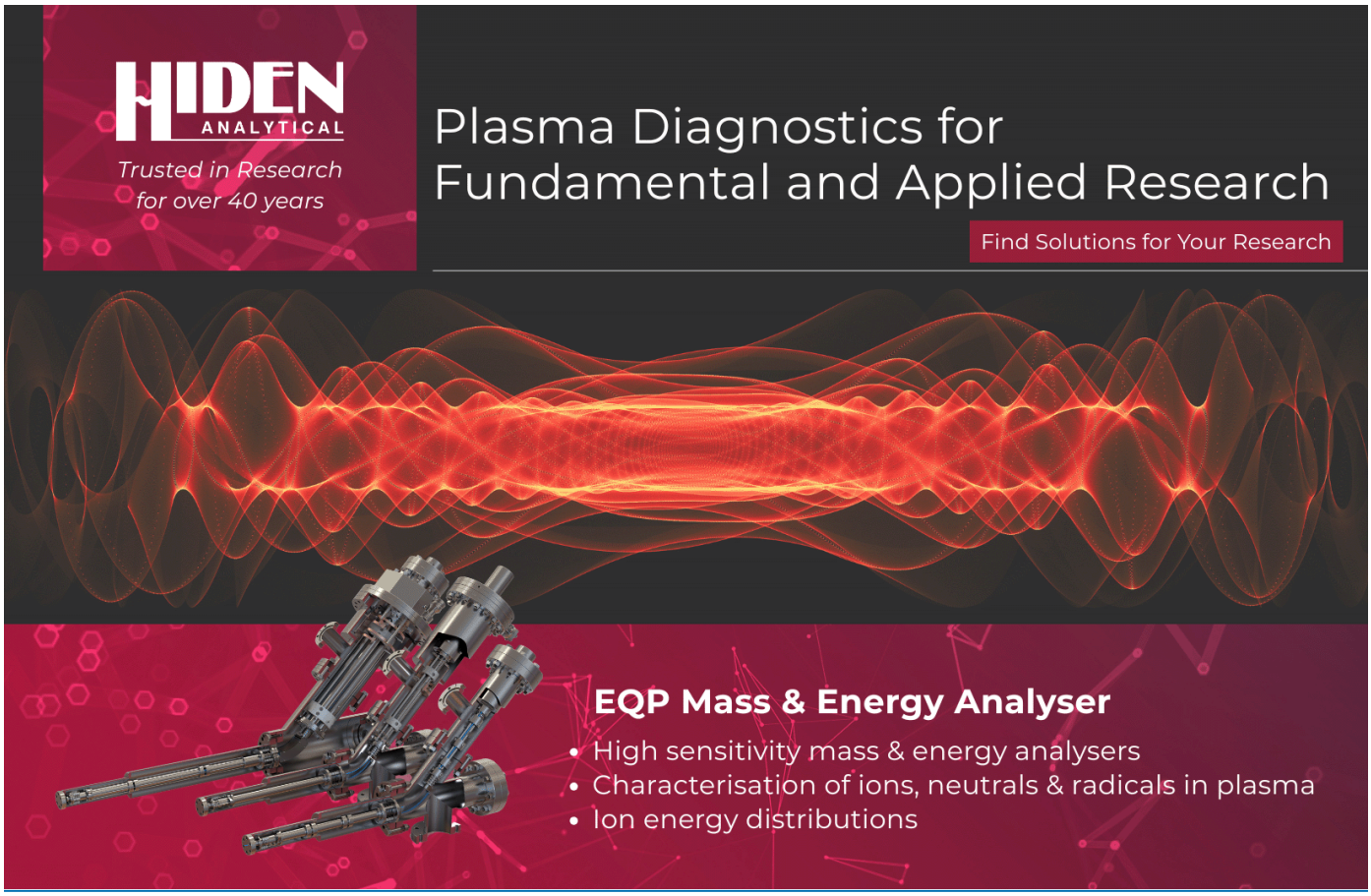
Effect of the magnetic field on the electron kinetics under AC/DC electric fields: benchmark calculations and electron cyclotron resonance

To cite this article: Tiago C Dias *et al* 2023 *Plasma Sources Sci. Technol.* **32** 095003

View the article online for updates and enhancements.

You may also like

- Global numerical simulation of chemical reactions in phosphate-buffered saline (PBS) exposed to atmospheric-pressure plasmas
Enggar Alfianto, Kazumasa Ikuse and Satoshi Hamaguchi
- A multi-ratio method for determination of the electric field from 2p states in transient argon discharges at atmospheric pressure
Zdenk Bonaventura, Zdenk Navrátil, Detlef Loffhagen et al.
- Mean Magnetic Field Generation in Sheared Rotators
Eric G. Blackman



This content was downloaded from IP address 216.73.216.56 on 19/11/2026 at 08:58

OPEN ACCESS
IOP Publishing
Plasma Sources Science and Technology
Plasma Sources Sci. Technol. **32** (2023) 095003 (16pp)
https://doi.org/10.1088/1361-6595/acf343

Effect of the magnetic field on the electron kinetics under AC/DC electric fields: benchmark calculations and electron cyclotron resonance

Tiago C Dias[1,*], **Carlos D Pintassilgo**[1,2] **and Vasco Guerra**[1]

[1] Instituto de Plasmas e Fusão Nuclear, Instituto Superior Técnico, Universidade de Lisboa, Lisboa, Portugal
[2] Departamento de Engenharia Física, Faculdade de Engenharia, Universidade do Porto, Porto, Portugal

E-mail: tiago.c.dias@tecnico.ulisboa.pt

Received 29 March 2023, revised 5 August 2023
Accepted for publication 23 August 2023
Published 4 September 2023

Abstract

This work presents a numerical study of the electron kinetics under AC/DC electric fields and DC magnetic fields crossed at arbitrary angles. The physical phenomena are studied both in model gases (Reid-ramp and Lucas–Saelee) and in real gases (N_2 and Ar). The simulations are carried out with an upgraded version of the Monte Carlo open-source code LoKI-MC. The code is compared against several independent benchmark calculations available in the literature. In addition, new benchmark calculations for electron kinetics solvers are produced in conditions of coexistent AC electric and DC magnetic fields, accounting for the effect of the crossing angle between the fields and discriminating the evolution along the AC cycle. The role of the magnetic field is discussed, distinguishing the configurations with DC and AC electric fields. In DC electric fields, the oscillatory motion caused by the magnetic field decreases the efficiency of the electron acceleration, which manifests on the power absorbed by the electric field and on the electron mean energy. Notably, an exceptional behavior is found in Ar for small regions of E/N and B/N, where: for constant B/N, the mean energy decreases with increasing E/N; and, for constant E/N, it increases with increasing B/N. These phenomena were firstly reported by Ness and Makabe in 2000 and are now confirmed by means of Monte Carlo simulations. In AC electric fields, when the magnetic field value is such that the electron cyclotron frequency is similar to the angular frequency of the electric field, the synchronization of the cyclotron motion with the electric field enhances electron acceleration, through the well-known electron cyclotron resonance. However, for conditions where the mean collision frequency is much higher than the cyclotron frequency, the synchronization tends to breakdown and the magnetic field is detrimental for the electron acceleration, as in the DC electric field case.

* Author to whom any correspondence should be addressed.

Original Content from this work may be used under the terms of the Creative Commons Attribution 4.0 licence. Any further distribution of this work must maintain attribution to the author(s) and the title of the work, journal citation and DOI.

 © 2023 The Author(s). Published by IOP Publishing Ltd

Supplementary material for this article is available online

Keywords: electron kinetics, magnetic field, benchmark, electron cyclotron resonance, Monte Carlo solver, open-source, LoKI-MC

(Some figures may appear in colour only in the online journal)

1. Introduction

Electrons play a fundamental role in the reactivity of low-temperature plasmas (LTP), since they transfer the energy gained from the electric field to the heavy species through a manifold of collisional channels. Therefore, an accurate description of the electron kinetics is necessary for a precise modeling of LTP, both for studies more focused on the plasma fluid dynamics and on the plasma chemistry.

The electron kinetics in LTP can be described by solving numerically the differential electron Boltzmann equation (EBE) or by tracking the stochastic motion of a representative ensemble of electrons using Monte Carlo (MC) techniques. Publicly available simulation tools based on either approach were developed in the last decades, for the benefit of the LTP community. Some examples are BOLSIG+ [1], EEDF [2], BOLOS [3], LoKI-B [4, 5], MultiBolt [6], METHES [7], Magboltz [8], Betaboltz [9], particle_swarm [10] and LoKI-MC [11]. The first four codes rely on a low-anisotropy approximation to solve the EBE, keeping only two terms in an expansion of the electron distribution in Legendre polynomials over the velocity space [12], which may be inaccurate when the inelastic collisions are strong or when the electric field is high [13]; MultiBolt is a multi-term solver (up to ten terms); and the latter five codes use MC integration techniques [14].

The LisbOn KInetics Monte Carlo (LoKI-MC) was recently developed by our group, aiming to provide the community a general and flexible electron kinetics solver that does not depend on the two-term approximation, distributed as open-source [11]. Some of its interesting features are: (i) straightforward insertion of gas internal levels (electronic, vibrational and rotational) and, accordingly, of superelastic and stepwise processes; (ii) possibility of describing anisotropic scattering in any collision kind [15]; (iii) inclusion of the thermal motion of the gas molecules, allowing to describe correctly the electron swarm kinetics at low E/N; (iv) calculation of the electron power balance over the various collisional channels.

The first version of LoKI-MC addressed only configurations with constant electric field and null magnetic field. However, the study of the electron kinetics under the simultaneous influence of electric and magnetic fields is relevant not only from the theoretical point of view, but also due to the practical applications on the modeling of LTP, such as: magnetron sputtering [16], plasma propulsion [17, 18] and inductively coupled discharges [19]. The theoretical efforts made in the recent decades are reviewed in [20–23]. The electron transport in these conditions has been studied in various gases, e.g.: Ar [24–26], CH_4 [8, 24, 27, 28], O_2 [23, 29], N_2 [30–32] and CF_4 [22]. Although the literature is relatively vast, to the best of our knowledge, the community is still lacking a flexible electron kinetics open-source solver, not depending on the low-anisotropy assumption, able to easily address such configurations. Herein, we extend the formulation implemented in LoKI-MC to AC/DC electric fields together with DC magnetic fields crossed at arbitrary angles.

The implementation of this significant additional feature requires an extensive benchmark/verification, besides the one already done in our previous work for DC electric fields [11]. The benchmark procedure for the verification of electron kinetics solvers is very well established in the LTP community. The use of gas models with analytical cross sections is fundamental to assure that the differences between the results obtained with different codes/formulations do not stem from the input data. The most popular ones are the Reid-ramp model [14] and the Lucas–Saelee model [33]. Albeit simple, they can capture the main features evidenced in real gases, while showing the limitations of the low-anisotropy approximation. Along the last decades, two groups from Australia [34–36] and Serbia [20, 23, 37, 38] made very important contributions to the publication of reference calculations in diverse conditions, using either MC or multi-term formulations. For the conditions of interest in this work, some examples of such calculations are: (i) AC electric and null magnetic fields [34, 35]; (ii) DC electric and DC magnetic fields [36–38]; (iii) AC electric and DC magnetic fields [23].

The purpose of the present work is clear and threefold: (i) present and verify an upgraded version of LoKI-MC, accounting for DC magnetic and AC/DC electric fields, comparing it against previous independent benchmark calculations, reinforcing the confidence on the present code and on the past calculations; (ii) extend the set of benchmarks available in the literature to assess the influence of other physical parameters, specially in conditions involving coexistence of AC electric fields and DC magnetic fields; (iii) gain insight into the underlying physics of the electron swarm kinetics in these configurations, with emphasis on the phenomenon of electron-cyclotron resonance (ECR). The kinetic effects are explored not only in the Reid-ramp and Lucas–Saelee models, but also in real gases, both molecular (N_2) and atomic (Ar). The updates in LoKI-MC discussed in this work are included in the open-source distribution of the code and are freely available to the community [11].

This paper is organized as follows: section 2 summarizes briefly the algorithm employed in LoKI-MC; section 3

presents the results using model and real gases, in conditions of AC/DC electric fields and DC magnetic fields, and discusses the physical phenomena involved; section 4 closes this work with the main conclusions and prospects for future work.

2. LoKI-MC

LoKI-MC simulates the electron transport in a background gas, under the influence of electric and magnetic fields, by following the stochastic trajectories in phase space of a representative ensemble of N_e electrons [11]. Electrons move in an unbounded environment, performing series of free flights interrupted by elastic, inelastic or superelastic collisions with gas molecules. The collisions are sampled using the null-collision technique [39], where the times between collisions are calculated with a constant trial collision frequency ν' which must satisfy

$$\nu' \geqslant \max_{\text{all } v_r}\{\nu_T(v_r)\}\ , \tag{1}$$

being $\nu_T(v_r)$ the total collision frequency for a given relative speed v_r between the electron and the gas molecule. During the simulation, the information of the electron trajectories is stored in order to calculate distribution functions, transport coefficients and other relevant quantities. The methods used in LoKI-MC are detailed in [11]. Here, we summarize the main steps to simulate the evolution of each electron in the ensemble, focusing on the improvements relatively to [11]:

1. The time-interval after which the next collision will occur (t_c) is calculated by mapping an uniform random number p_t in the $]0,1[$ range into a Poisson distribution [40]: $t_c = -\frac{\ln p_t}{\nu'}$.
2. The electron position (**r**) and velocity (**v**) are advanced during t_c by integrating analytically the Newton equations of motion, under the influence of an electric field (**E**) and a magnetic field (**B**):

$$m_e\frac{\mathrm{d}\mathbf{v}}{\mathrm{d}t} = -e(\mathbf{E}+\mathbf{v}\times\mathbf{B}) \quad , \quad \frac{\mathrm{d}\mathbf{r}}{\mathrm{d}t} = \mathbf{v}\ , \tag{2}$$

   where e and m_e are the electron charge and mass, respectively. In the current version of LoKI-MC, **E** can be either AC or DC, **B** is constant, and the fields are crossed at an arbitrary angle $\Psi \in [0°, 180°]$:

$$\mathbf{E}(t) = (E_{x,0}\mathbf{e_x} + E_{z,0}\mathbf{e_z})\cos(\omega t) \quad , \quad \mathbf{B} = B\mathbf{e_z}\ , \tag{3}$$

   where $\omega = 2\pi f$ is the angular frequency of the field, $E_{x,0} = \sin\Psi E_0$, $E_{z,0} = \cos\Psi E_0$ and E_0 is the electric field amplitude. The analytical solutions for the propagation of **r** and **v**, from an time-instant t_0 up to $t_0 + t_c$, are presented in appendix A, together with other particular cases, such as $\omega = 0$, $B = 0$ and $\omega = \Omega = eB/m_e$ (ECR). This step constitutes a significant update in comparison with the previous release of the code [11], where only DC **E** fields were accounted for. Take note that the angle Ψ could be taken between 0° and 90°, since extension to 90° and 180° can be made through use of symmetry properties [41]. However, we let it lie between 0° and 180° since the complexity of the equations of motion does not change.
3. The random velocity **V** of the target gas molecule is determined from a Maxwell–Boltzmann distribution at the gas temperature.
4. Knowing **v** and **V**, the likelihoods of the occurrence of the various collision kinds $\mathcal{K}$, $P_\mathcal{K}$, are calculated as: $P_\mathcal{K} = \frac{\nu_\mathcal{K}(v_r)}{\nu'} = \frac{n^s_\mathcal{K}\sigma_\mathcal{K}(v_r)v_r}{\nu'}$, where $n^s_\mathcal{K}$ is the density of the target species s and $\sigma_\mathcal{K}(v_r)$ is the collision cross section. Moreover, due to the overestimation of the collision frequency associated with the null-collision technique, a null-collision process must be added with probability $P_{\text{null}} = \frac{\nu_{\text{null}}(v_r)}{\nu'} = \frac{\nu_T(v_r)-\nu_\mathcal{K}(v_r)}{\nu'}$. Then, the collision type is chosen based on the calculated probabilities and the generation of a random number between 0 and 1. If a null collision is chosen, no real interaction occurs and step 5 is skipped.
5. Depending on the collision type, the change of the velocity vector is calculated based on the generation of random numbers and the conservation laws for energy and momentum (see sections 2.5 and 2.6 of [11] for more details). The angular scattering in any collision type can be either isotropic or anisotropic, as detailed in [15].

These steps are repeated multiple times for each electron until the simulation concludes.

To keep the number of electrons constant in the simulation, when there is an ionization event, a randomly chosen electron is removed, and when there is an attachment, a random electron from the ensemble is copied. This technique confers stability to the code and does not affect the average properties of the ensemble [42, 43]. However, the renormalization must be performed with care; in particular, it should be done according to the distribution of electrons that were previously in the ensemble, plus the newly-born electrons from ionization events, less the attached electrons. In the first version presented in [11], the newly-born electrons were being replaced by a random electron from the ensemble, which is not correct, since it gives a preferential weight to this kind of electrons. This imprecision was creating slight differences from multi-term results [6], for conditions where ionization is dominant (e.g. in Ar, for $E/N \gtrsim 500$ Td, see figure 5 of [11]). With the correct renormalization of the electron number, the differences have vanished.

Since the time interval t_c is random and different for each electron, the evolution of the ensemble is not synchronized, which poses challenges in sampling electron properties required for calculating the swarm coefficients. In the previous version of LoKI-MC [11], this issue was circumvented by generating a single random time-step and applying it uniformly to all electrons. Nevertheless, it was observed that while this approach yields the correct average values, it introduces significant statistical fluctuations, leading to longer computation times, specially when inelastic processes are dominant. Therefore, in this work we relax that approximation and allow

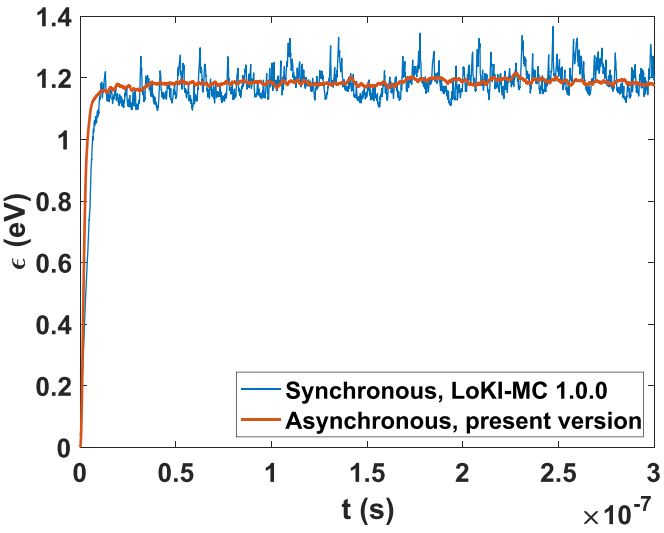


Figure 1. Temporal evolution of the electron swarm energy (ϵ) in a simulation involving 10^4 electrons in N_2 at $E/N = 50$ Td, comparing the synchronous and asynchronous advancement of electrons.

the electrons to evolve freely in time until specific time-instants where they are once again synchronized (see chapter 10.3.3 of [44] for more details).

It is crucial to keep the time interval between synchronizations sufficiently low to ensure that the renormalization of the electron distribution described in the paragraph above involves electrons at similar times. If the time interval is too large, systematic errors may occur in transport coefficients depending on the electron positions, which are not ergodic in time. To address this, we set the time interval as a multiple, $\mathcal{N}_{\text{sync}}$, of the constant trial collision frequency ν': $\Delta t_{\text{sync}} = \mathcal{N}_{\text{sync}}/\nu'$. Notably, no systematic deviations were found for synchronization factors $\mathcal{N}_{\text{sync}}$ between 0.01 and 10, even in cases with strong ionization. The default value of $\mathcal{N}_{\text{sync}} = 1$ ensures good computational efficiency, but users have the flexibility to change it in the setup file. The sampling of electron positions and velocities is performed at each synchronization instant. Alternatively, users can specify in the setup file to sample these properties only at arbitrary multiples of synchronization points.

Figure 1 illustrates the temporal evolution of the electron swarm energy (ϵ) in a simulation involving 10^4 electrons in N_2 at $E/N = 50$ Td, comparing the synchronous (old) and asynchronous (present) advancement of electrons. The implementation of asynchronous electron advancement in the present version significantly enhances the statistical precision of the results.

The techniques used to calculate the electron swarm parameters from the spatiotemporal evolution of the swarm are detailed in section 2.6 of [11]. For the determination of the transport coefficients, we distinguish between 'flux' and 'bulk' components, which may differ when non-conservative processes are significant [20]. The flux drift velocity $v^f_{d,i}$ and diffusion tensor D^f_{ij} $(i,j = x,y,z)$ are determined from the averages over the instantaneous positions (r_i) and velocities (v_i) of the electrons in the swarm [20]:

$$v^f_{d,i} = \langle v_i \rangle \ , \tag{4}$$

$$D^f_{ij} = \langle r_i\, v_j \rangle - \langle r_i \rangle \langle v_j \rangle \ . \tag{5}$$

The bulk drift velocity $v^b_{d,i}$ and diffusion tensor D^b_{ij} are defined relatively to the swarm center-of-mass $\langle r_i \rangle$ [7, 36],

$$v^b_{d,i} = \frac{\mathrm{d}}{\mathrm{d}t}\langle r_i \rangle \ , \tag{6}$$

$$D^b_{ij} = \frac{1}{2}\frac{\mathrm{d}}{\mathrm{d}t}\left(\langle r_i\, r_j \rangle - \langle r_i \rangle \langle r_j \rangle\right) \ , \tag{7}$$

and can be obtained from linear regressions to the temporal evolution of $\langle r_i \rangle$ and $\langle r_i\, r_j \rangle - \langle r_i \rangle \langle r_j \rangle$, respectively.

3. Results and discussion

This section presents and discusses results of the electron swarm kinetics in the presence of a magnetic field. The MC simulations are run with 10^4–10^6 electrons and each electron performs typically between 10^4 and 10^6 collision-free flights. All simulations assume isotropic collisional scattering and consider a gas density $N = 3.54 \times 10^{22}\,\mathrm{m}^{-3}$ and gas temperature $T_g = 300\,\mathrm{K}$, unless mentioned otherwise. However, the results presented here are independent of the value used for the gas density, with exception of section 3.2.

In this work, we consider two well-known model gases: Reid-ramp [14] and Lucas–Saelee [33]. The Reid-ramp model [14] is constituted by the following elastic and excitation cross sections:

$$\begin{cases} \sigma_{\text{el}} &= 6 \times 10^{-20}\,\mathrm{m}^2 \\ \sigma_{\text{exc}} &= (u - 0.2) \times 10^{-19}\,\mathrm{m}^2 \end{cases} \ , \tag{8}$$

where the electron energies u are given in eV and the threshold of the excitation cross section is 0.2 eV. The Lucas–Saelee [33] model is composed by elastic, excitation and ionization cross sections:

$$\begin{cases} \sigma_{\text{el}} &= 4u^{-1/2} \times 10^{-20}\,\mathrm{m}^2 \\ \sigma_{\text{exc}} &= 0.1(1-F)(u-15.6) \times 10^{-20}\,\mathrm{m}^2 \\ \sigma_{\text{ion}} &= 0.1F(u-15.6) \times 10^{-20}\,\mathrm{m}^2 \end{cases} \ , \tag{9}$$

where the threshold of the excitation and ionization cross sections is 15.6 eV, and $F \in [0,1]$ is a parameter controlling the intensity of ionization. In the Reid-ramp model, the heavy species mass is $M = 4$ a.m.u., whereas in Lucas–Saelee, $M = 1000\, m_e$. In both models, the thermal motion of the heavy species is not considered. Notice that Ness and Robson [45] extended the Lucas–Saelee model to include as well an attachment process. For simplicity, we do not consider it here, as LoKI-MC already passed this benchmark test in conditions of DC electric field and null magnetic field [11].

For both DC and AC electric fields, we start by benchmarking LoKI-MC results against previously published calculations, using the Reid-ramp and Lucas–Saelee model gases. We also employ the Reid-ramp model in different conditions from those available in the literature, exploring the angle between the fields and evidencing that the dynamics is ruled only by density-reduced quantities. These results constitute additional benchmark calculations for verification of future codes. Then, we study the electron kinetics in real gases—N_2 and Ar—using the cross-section sets available at the IST-Lisbon database of LXCat [46]. For more details on these cross sections, see sections 4.4.2 and 4.5 of [11]. Lastly, let us note that the present calculations also agree very well with the available benchmark results for AC electric fields and null magnetic fields, as shown in appendix B.

3.1. DC electric field

This subsection studies the effect of the magnetic field together with a DC electric field. First, we need to assure that LoKI-MC passes the typical benchmark tests. Figure 1 shows a comparison between the present calculations and the MC results of Raspopovic *et al* [37], using the Reid-ramp model, for $E/N = 12$ Td (1 Td = Townsend $= 10^{-21}$ Vm^2) and different B/N (1 Hx = Huxley $= 10^{-27}$ Tm^3), with the electric field **E** perpendicular to the magnetic field **B** ($\Psi = 90°$). The mean energy $\langle\epsilon\rangle$ and the non-null components of the drift velocity $v_{d,i}$ and the diffusion matrix ND_{ij} agree remarkably well with [37]. For the reference frame used in this work, the Hall diffusion coefficient is defined as: $D_{\text{Hall}} = -(D_{xy} + D_{yx})$ [36]. For an extended interpretation of these results, the reader is referred to [36, 37]. We point out that, with increasing B/N, the electrons become magnetized and (i) the electron energy is strongly reduced due to a smaller efficiency of the electric-field acceleration, (ii) the drift velocity along **E** decreases and a component along $\mathbf{E}\times\mathbf{B}$ arises, (iii) the diffusion perpendicular to **B** is dampened, while in the parallel direction barely changes.

Note that, since the Reid-ramp model conserves the number of electrons, flux and bulk components are equivalent. To verify the effect of non-conservative processes, as well as the angle between **E** and **B**, we employ the Lucas–Saelee model for different ionization factors F and angles Ψ, comparing with the MC results of Dujko *et al* [38]. The electron mean energy $\langle\epsilon\rangle$, bulk drift speed $\|v_d^b\|$ and ionization coefficient k_{ion} are shown in figure 3, as a function of Ψ, for $E/N = 10$ Td, $B/N = 200, 1000$ Hx and $F = 0, 0.5, 1$. There is an excellent agreement between the present results and the ones reported in [38]. Although not shown here, the accordance in the three components of $\mathbf{v_d^b}$ is also very good[3]. Concerning the influence of ionization, we find that with increasing F, $\langle\epsilon\rangle$ decreases, while $\|v_d^b\|$ and k_{ion} increase. Additionally, as in the previous case, a higher B/N leads to a lower $\langle\epsilon\rangle$. The effect of **B** is null/maximal, when **B** is parallel/perpendicular to **E**, as expected. The flux drift speed $\|v_d^f\|$ is not shown here but, for all values of F, is identical to $\|v_d^b\|$ for $F = 0$, as it does not depend on the change of the electron number.

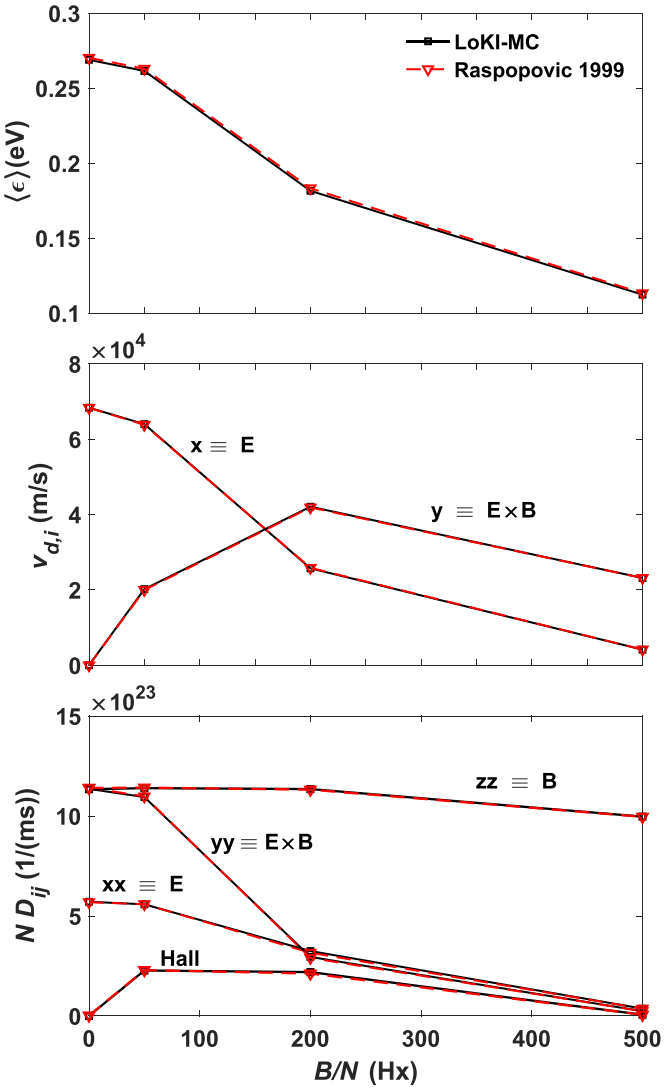


Figure 2. Electron mean energy $\langle\epsilon\rangle$, drift velocity $v_{d,i}$ and diffusion coefficients ND_{ij}, in the Reid-ramp model, as a function of B/N, for $E/N = 12$ Td and $\Psi = 90°$. The calculations are compared with the MC results of Raspopovic *et al* [37].

After the verification in model gases shown in figures 2 and 3, we focus now on the electron swarm kinetics in real gases (N_2 and Ar), keeping **E** perpendicular to **B** ($\Psi = 90°$). Figures 4(a) and (b) present the electron mean energy $\langle\epsilon\rangle$ and reduced Townsend coefficient α/N, as function of E/N and $B/N = 0$–3000 Hx, for N_2 and Ar, respectively. For N_2, the calculated values of α/N are in quite good agreement with the measurements of Heylen and Dargan [47]. Notice that the same comparison between calculated and measured α/N has been performed with similar success in previous works [30, 31]. In both gases, the magnetic field decreases dramatically the energy of the electrons and, consequently, α/N.

Figures 5(a) and (b) illustrate $\langle\epsilon\rangle$ in wider conditions of E/N and B/N, for N_2 and Ar, respectively. The variation of

[3] Since Dujko *et al* [38] use a different reference frame (D), the results need to be converted to the one used in this work: $\mathbf{e_x} = \cos\Psi\mathbf{e_y^D} - \sin\Psi\mathbf{e_z^D}$; $\mathbf{e_y} = \mathbf{e_x^D}$; $\mathbf{e_z} = -\sin\Psi\mathbf{e_y^D} - \cos\Psi\mathbf{e_z^D}$.

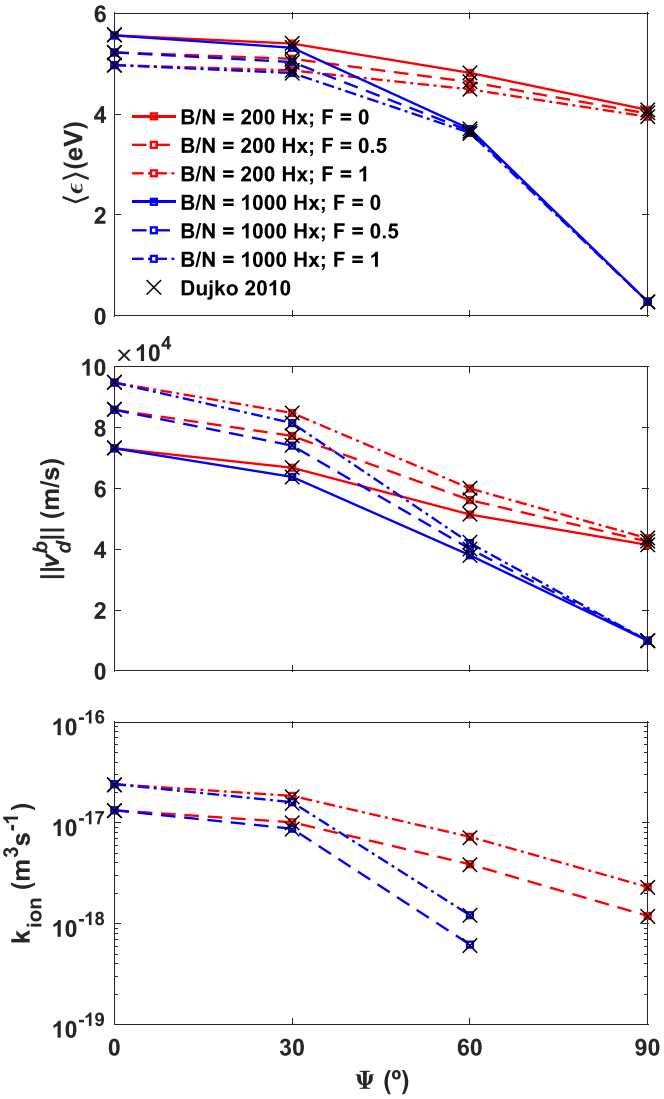


Figure 3. Electron mean energy $\langle\epsilon\rangle$, bulk drift speed $\|v_d^b\|$ and ionization coefficient k_{ion}, in the Lucas–Saelee model, as a function of Ψ, for $E/N = 10$ Td, $B/N = 200, 1000$ Hx and $F = 0, 0.5, 1$. The calculations are compared with the MC results of Dujko *et al* [38].

$\langle\epsilon\rangle$ in N_2 exhibits the expected behavior: for constant B/N, it increases monotonically with E/N, while for constant E/N, it decreases with increasing B/N. In Ar, the trend is generally similar, except for local regions where the opposite occurs: (i) $\langle\epsilon\rangle$ decreases with increasing E/N and (ii) $\langle\epsilon\rangle$ increases with increasing B/N. The first feature is well observed for $B/N = 1000$ Hx in the 4 Td region. The second feature is evident in the crossing between the curves of $B/N = 5000$ and 10 000 Hx.

These interesting phenomena were reported for the first time in 2000 by Ness and Makabe [25]. Nevertheless, to the best of our knowledge, until now, it has not been confirmed by other authors, even though Ness and Makabe conclude the manuscript stating that the finding should be verified by an independent study, such as a MC simulation investigation. For a detailed discussion of the physics behind this effect, the reader is referred to [25]. In short, the exceptional behavior in argon occurs due to the rapidly increasing magnitude of the elastic cross section after the Ramsauer minimum, from ∼0.25 up to 10 eV, followed by the sudden appearance of strong inelastic processes after ∼11 eV, as illustrated in figure 6. For constant B/N, when E/N is increased, electrons are accelerated to energies where the collisionality increases significantly. For null and weak magnetic fields, this causes only a decrease in the $\langle\epsilon\rangle$ slope. However, for $B/N \gtrsim 500$ Hx, the magnetic field cooling is contributing somehow to enhance this effect, leading to small transient regions where $\langle\epsilon\rangle$ decreases with E/N. The transient increase of $\langle\epsilon\rangle$ with increasing B/N can be explained in a similar manner [25].

The black-dashed curves represent the MC solutions with $B = 0$ and an effective AC electric field with the corresponding cyclotron frequency, $\omega/N = \Omega/N = eB/(Nm_e)$, and $E_{\text{rms}}/N = E_{\text{DC},B\neq0}/N$. The similarity of these curves with the ones in the presence of a magnetic field shows that, from the energetic point of view, the effect of the magnetic field is approximately equivalent to the introduction of an AC component in the electric field, as expected (cf equation (11) further below).

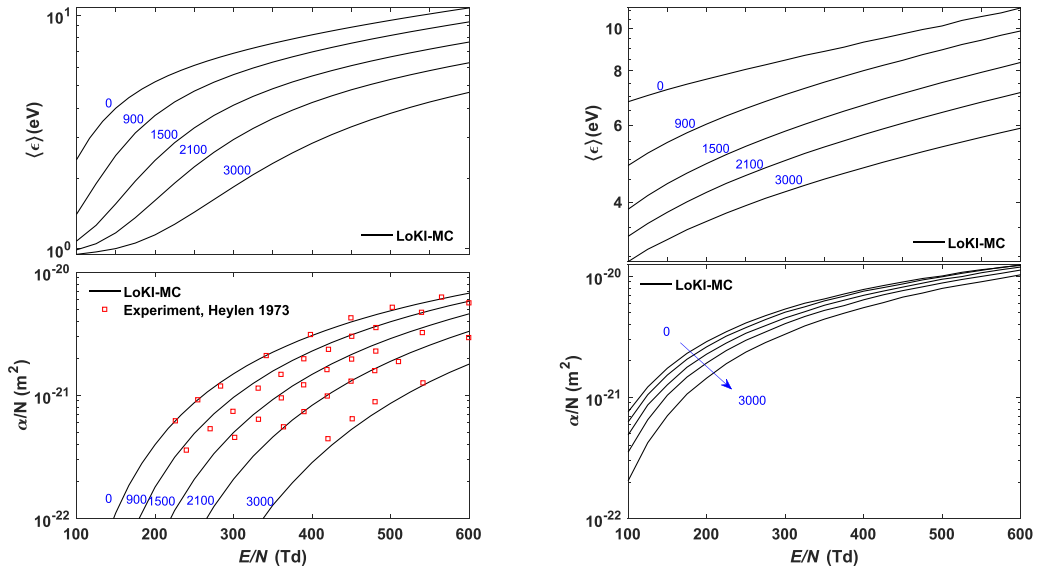


Figure 4. Electron mean energy $\langle\epsilon\rangle$ and reduced Townsend coefficient α/N, in N_2 (a) and Ar (b), as a function of E/N, for various B/N. For N_2, α/N is compared against experiments [47].

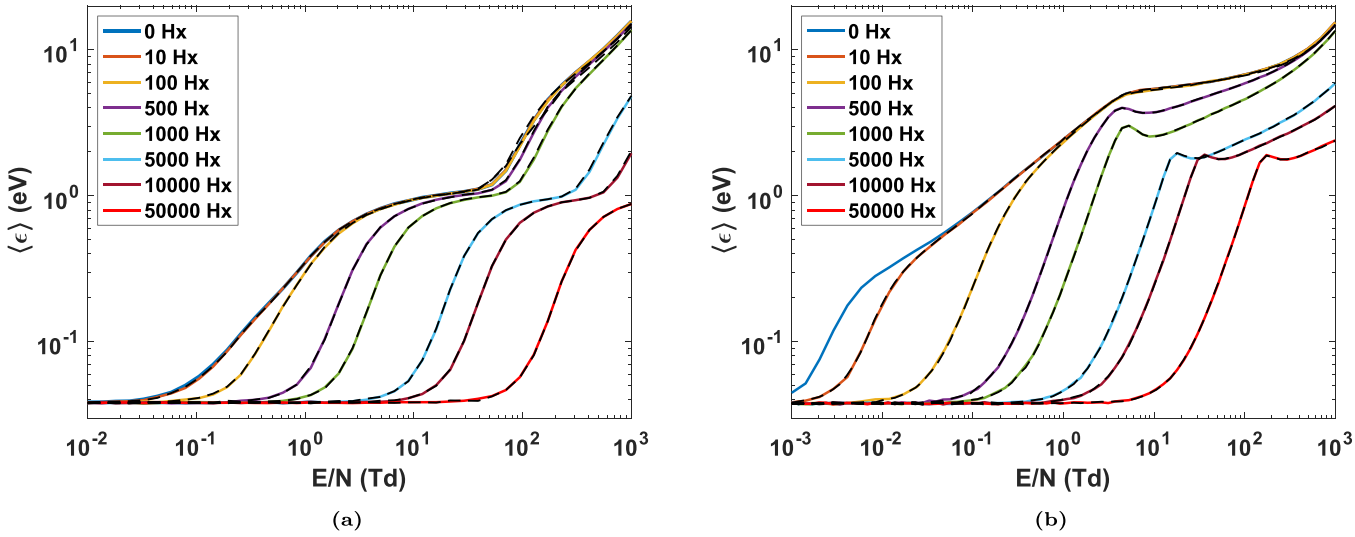


Figure 5. Electron mean energy $\langle\epsilon\rangle$, in N_2 (a) and Ar (b), as a function of E/N, for $B/N = 0$–50 000 Hx. In N_2, the results for $B/N = 0$ and 10 Hx are almost superposed. The black-dashed lines represent the results with null B and an effective AC E-field.

Such behavior could also be predicted by inspecting the EBE, under a low-anisotropy expansion on spherical harmonics over the velocity space and on the limit of very high frequencies, where the solution of the isotropic component of the electron velocity distribution takes the same form in both AC electric fields and DC magnetic fields (for more details, see chapter 4.2.2 of [48]). However, at $B/N = 10$ and 100 Hx, the effective AC E-field leads to significantly different results. The deviations are particularly evident for N_2 at $E/N \gtrsim 30$ Td.

Figure 7 presents the relaxation of the electron swarm energy in N_2, for $E/N = 100$ Td and different B/N, and compares with the solutions using an effective AC electric field. For lower B/N, the AC field cannot capture neither the initial relaxation nor the mean steady-state value. When the cyclotron frequency Ω is much larger than the average frequency for energy relaxation ν_ϵ, the equivalence becomes very good. In the particular conditions of figure 7, ω/ν_ϵ is 5.2, 30.8, 95.9 and 6350, for $B/N = 100$, 500, 1000 and 5000, respectively. In any case, a proper implementation of the magnetic field should be always considered, in order to obtain a correct description of the transport properties, such as the diffusion coefficients and the drift velocity. The only aim of the present discussion is to provide insight into the effect of the magnetic field from the energetic point of view.

Lastly, figures 8(a) and (b) show the electron energy distribution functions (EEDF) at $E/N = 100$ Td and various B/N,

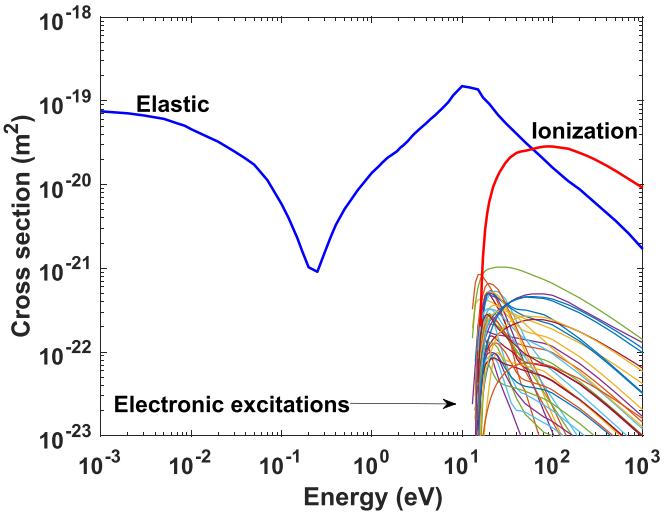


Figure 6. Electron-impact cross sections in Ar, available at the IST-Lisbon database of LXCat [46].

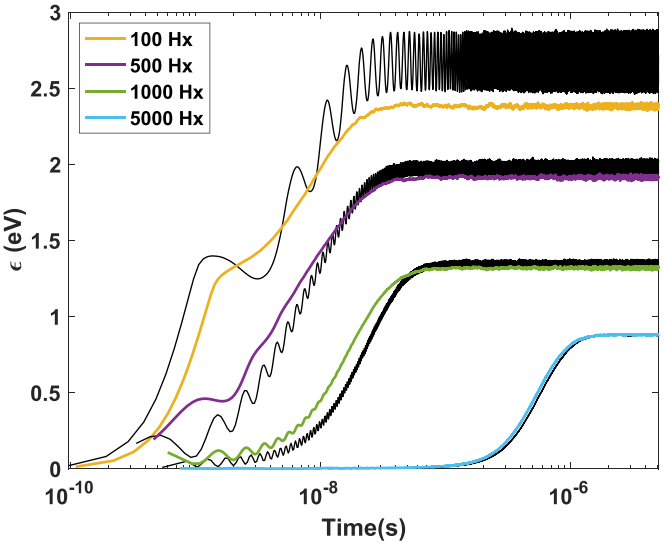


Figure 7. Temporal evolution of the electron swarm energy (ϵ) in N_2, for $E/N = 100$ Td and different B/N. The black curves represent the results with null B and an effective AC E-field.

together with the respective solution with an effective AC electric field and null magnetic field. The EEDFs evidence the remarkable decrease of the high energy electrons caused by the magnetic field, as well as the approximative equivalence between the magnetic field and effective AC electric field cases, failing more at lower B/N.

3.2. AC electric field: phenomenon of ECR

The impact of the magnetic field on the electron kinetics may be substantially different when the electric field is oscillatory. In particular, if the angular frequency $\omega = 2\pi f$ of the AC electric field is comparable to the electron cyclotron frequency $\Omega = eB/m_e$, the magnetic field can increase the efficiency of the electric-field acceleration, due to the well-known phenomenon of ECR [48, 49].

We start the analysis of the ECR process using the Reid-ramp model, with $\mathbf{E}$ perpendicular to $\mathbf{B}$ ($\Psi = 90°$). Contrarily to the previous subsection, the results are now dependent on the gas density N. Therefore, keep in mind that $N = 3.54 \times 10^{22}\,\mathrm{m}^{-3}$, unless stated otherwise. Moreover, for this model, the root-mean-squared reduced electric field is $E_{\mathrm{rms}}/N = 10$ Td. Figure 9 shows the electron mean energy $\langle\epsilon\rangle$ and reduced electric-field power $\langle P_E/N\rangle$, as a function of B/N, for different excitation frequencies f. The results are compared with the work by Dujko *et al* [23] and slight differences are found, specially at higher frequencies[4]. After a careful analysis, no specific reason has been found for this small disagreement. Such deviations may be due to slightly different conditions of electric field and/or gas density; or inaccuracies due to the unavoidable truncation of a multi-term expansion, which is unlikely since in [23] four anisotropy degrees are considered and it was checked this gives a good accuracy. In principle, these differences do not stem from LoKI-MC, since they exist even at $B = 0$ and our code is successfully benchmarked in these conditions (cf appendix B). Furthermore, the resonance peaks at high frequencies calculated using LoKI-MC tend to the solution of a DC electric field with $E_{\mathrm{DC}}/N = E_0/N/2 = E_{\mathrm{rms}}/N/\sqrt{2}$ and null magnetic field, which is the expected result and constitutes an additional verification test, as discussed below.

The electron response to the magnetic field varies significantly with the frequency f of the electric field. For $f = 50$ MHz, $\langle\epsilon\rangle$ and $\langle P_E/N\rangle$ decrease monotonically with B/N; for $f = 100$ MHz the ECR starts to play a role; and for $f \geqslant 200$ MHz the resonance curve is clear. To understand this behavior, we need to examine closely the physics of ECR This is better understood if we decompose the linearly-oscillating electric field as a sum of right-hand and left-hand circular electric-fields ($\mathbf{E}_{\mathrm{RH}}$ and $\mathbf{E}_{\mathrm{LH}}$) [48]:

$$\mathbf{E}(t) = E_0\cos(\omega t)\mathbf{e_x} = \mathbf{E}_{\mathrm{RH}} + \mathbf{E}_{\mathrm{LH}} = \frac{E_0}{2}\left(\cos(\omega t)\mathbf{e_x} + \sin(\omega t)\mathbf{e_y}\right) + \frac{E_0}{2}\left(\cos(\omega t)\mathbf{e_x} - \sin(\omega t)\mathbf{e_y}\right), \quad (10)$$

where it is considered that $\Psi = 90°$. The cyclotron motion induced by the magnetic field (along $\mathbf{e_z}$) occurs in the xy plane in the right-hand direction. When the electron cyclotron frequency Ω is equal to the angular frequency ω, the electrons can be continuously accelerated by $\mathbf{E}_{\mathrm{RH}}$, leading to the ECR However, when ω is low compared to the collision frequency ν, the collisions with the heavy-species tend to breakdown the synchronous motion and ECR is negligible.

Additional explanation of the effects reported in figure 9 can be obtained from the analysis of the angle between the

[4] Notice that the results of P_E from [23] (figure 10) need to be divided by $10\sqrt{2}$, i.e. the amplitude of E/N in Td.

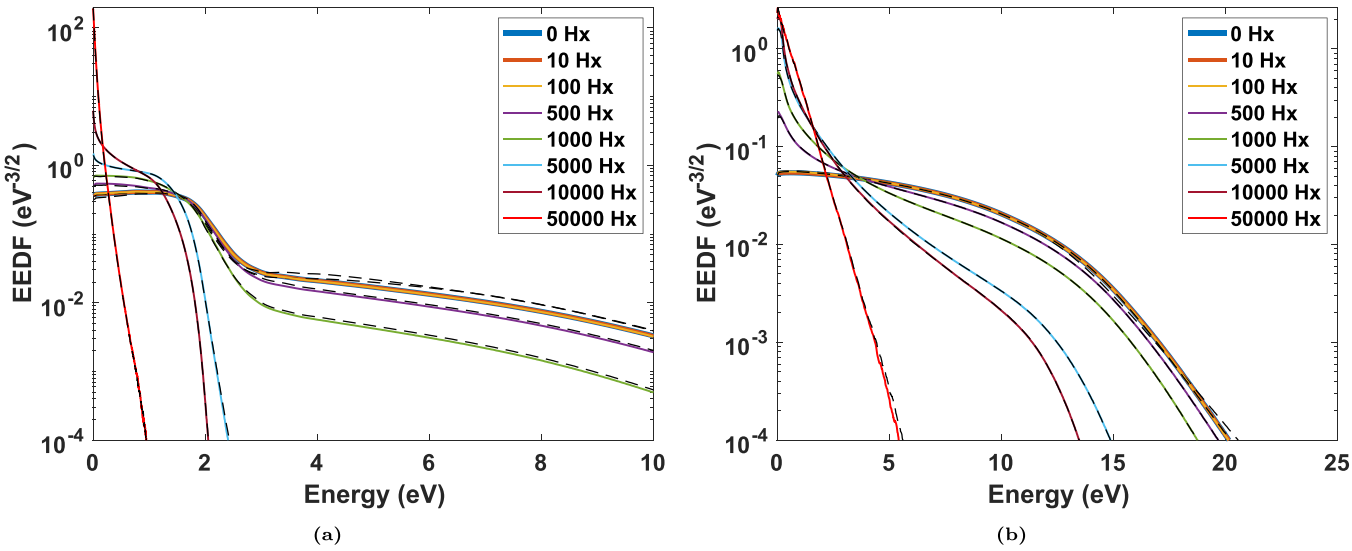


Figure 8. EEDFs in N_2 (a) and Ar (b), at $E/N = 100$ Td and $B/N = 0$–$50\,000$ Hx. The results for $B/N = 0, 10, 100$ Hx are almost superposed. The black-dashed lines represent the results with an effective AC E-field.

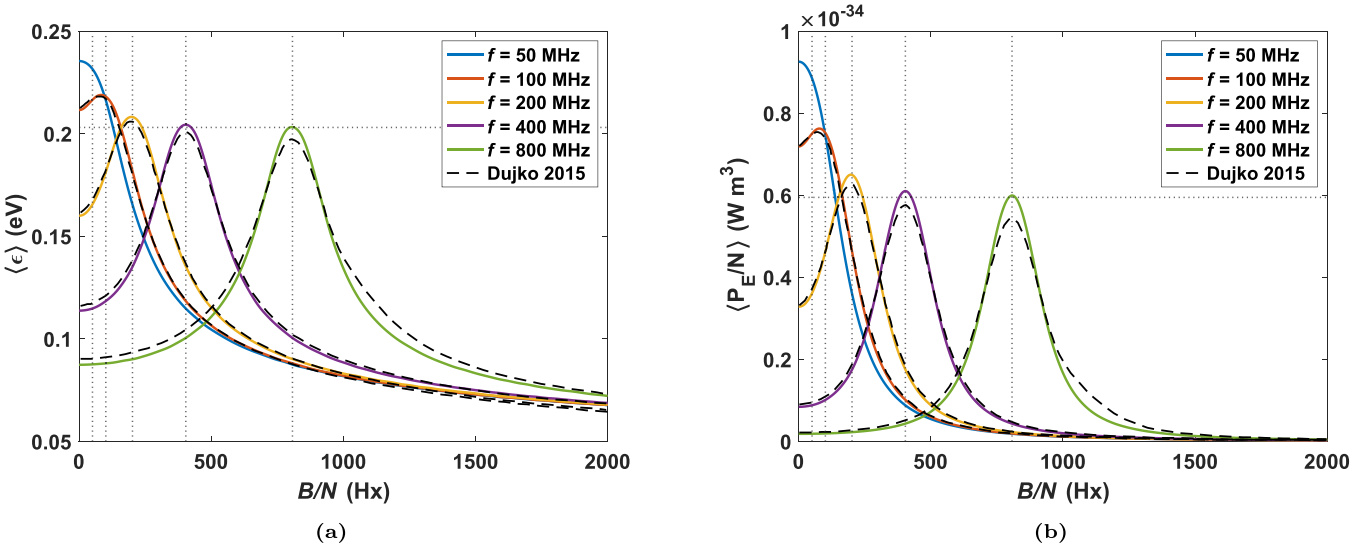


Figure 9. Electron mean energy $\langle\epsilon\rangle$ (a) and reduced electric-field power $\langle P_E/N\rangle$ (b), as a function of B/N, for different excitation frequencies f, in the Reid-ramp model. The results are compared against [23], except for $f = 50$ MHz (value considered here to provide additional insight to the present study). Vertical dotted lines indicate the values of B/N for which ECR occurs. Horizontal dotted lines represent the calculations using a DC electric field with $E_{DC}/N = E_0/N/2 = 10/\sqrt{2}$ Td and null magnetic field, and should match the value at ECR for high frequencies.

electron drift velocity $\mathbf{v_d}$ and $\mathbf{E}_{RH}$, as shown in figure 10(a). At $f = 50$ MHz, the drift motion is still largely affected by collisions, causing significant deviations from optimal acceleration by $\mathbf{E}_{RH}$ (maximal at 180°). For this reason, for low frequencies, ECR is not beneficial, and adding a magnetic field only decreases the overall electron acceleration, as in the DC cases shown in section 3.1. For high frequencies, the oscillations decrease and $\mathbf{v_d}$ is mostly antiparallel to $\mathbf{E}_{RH}$; in this case, the electron acceleration is approximately equivalent to the one in a DC electric field with $E_{DC}/N = E_0/N/2$ and null B. This characteristic can be further confirmed in figure 11(a), showing the reduced power gained due to the right-circular electric field, $P_{E_{RH}}/N = -e\mathbf{v_d}\cdot\mathbf{E}_{RH}/N$, along the AC period. On the other hand, the angle between $\mathbf{v_d}$ and $\mathbf{E}_{LH}$ varies between 0° and 180° (see figure 10(b)), since $\mathbf{E}_{LH}$ rotates in the opposite direction of the cyclotron motion. Moreover, figure 11(b) shows that for higher frequencies where ECR is dominant, the average power due to $\mathbf{E}_{LH}$ is approximately null.

For a complementary analysis of the results in figure 9, let us examine the reduced electric-field power considering

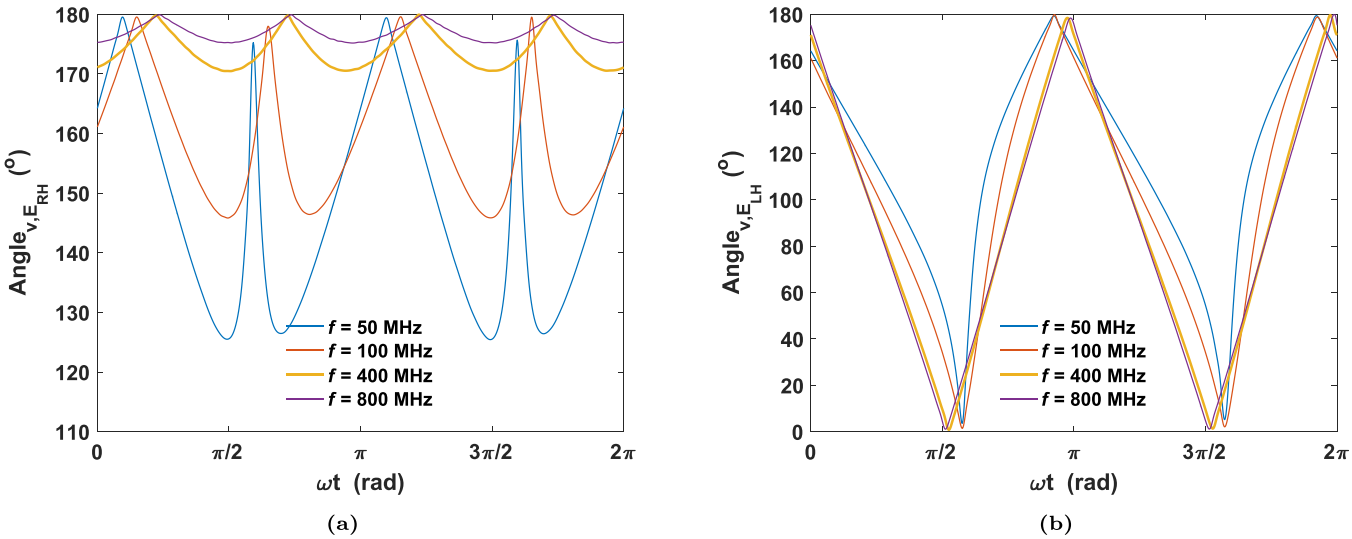


Figure 10. Angle between the electron drift velocity $\mathbf{v}_d$ and the right-hand (a) and left-hand (b) circular electric fields, along the AC period, in the Reid-ramp model.

a fluid (single velocity) formulation (see chapter 4.2 of [48] and [49]):

$$\left\langle \frac{P_E}{N} \right\rangle = \left\langle \frac{P_{E_{\mathrm{RH}}}}{N} + \frac{P_{E_{\mathrm{LH}}}}{N} \right\rangle = \frac{e^2}{4m_e} \left(\frac{k_m}{k_m^2 + (\omega/N - \Omega/N)^2} + \frac{k_m}{k_m^2 + (\omega/N + \Omega/N)^2} \right) \left(\frac{E_0}{N} \right)^2, \tag{11}$$

where $k_m = \nu_m/N$ is the rate coefficient for the total momentum transfer. In resonance conditions, the first term (RH) is dominant only when $\omega/N \gtrsim k_m$. For reference, table 1 presents the values of ω/N and $(\omega/N)/k_m^{\mathrm{typ}}$, in the Reid-ramp model, N_2 and Ar, for the different frequencies f used here and considering $N = 3.54 \times 10^{22}\,\mathrm{m}^{-3}$. The momentum-transfer rate-coefficient k_m^{typ} is calculated from the solution with $E_{\mathrm{DC}}/N = E_0/N/2$ and null B, typical of the resonance peak. As expected, in the Reid-ramp model, for $f = 100\,\mathrm{MHz}$, $(\omega/N)/k_m^{\mathrm{typ}} \sim 1$, which corresponds to the frequency where ECR starts to be relevant.

Figure 12 shows the mean energy in N_2 and Ar, as a function of B/N, for the same conditions as in the Reid-ramp model, except for $E_{\mathrm{rms}}/N = 100\,\mathrm{Td}$. The physical behavior is essentially the same as the one found in the Reid-ramp model, which reinforces the interest of this simple gas model in the study of fundamental physical phenomena. By comparison with table 1, we find that the resonant peak in Ar appears at slightly lower values of $(\omega/N)/k_m$ ($\sim$0.5) than in N_2 ($\sim$1.7), and this is related with the larger importance of elastic collisions in this gas. Furthermore, for both N_2 and Ar, the maximum of $\langle\epsilon\rangle$ at high frequencies is in accordance with the theoretically predicted value (indicated in the horizontal lines).

The Reid-ramp model can still be considered to study the influence of other physical parameters besides the electric field frequency f. In particular, until now the gas density has been fixed to $N = 3.54 \times 10^{22}\,\mathrm{m}^3$. Figure 13 shows the resonance curves of the energy and reduced power, for densities 10 times lower and higher than the default value, compensating f with the same factor, as to keep ω/N constant. The exact equivalence between these curves confirms that the relevant parameter for ECR is ω/N, as could be expected from the previous discussion and (11).

Finally, we analyze the ECR process when **E** and **B** are crossed with an arbitrary angle, varying Ψ from 0 to 180°, keeping $f = 400\,\mathrm{MHz}$, $N = 3.54 \times 10^{22}\,\mathrm{m}^3$ and $\omega = \Omega$. Figure 14(a) shows that the electron mean energy is maximal at $\Psi = 90°$ and the intervals $[0, 90]°$ and $[90, 180]°$ are symmetric, as expected [41]. Figures 14(b), (c) and (d), represent the electron drift velocity along an AC cycle, in 3D, xy plane and xz plane, respectively, for $\Psi = 0°, 30°, 60°$ and 90°. These figures evidence the non-perturbation of the motion by the magnetic field for $\Psi = 0°$, while for $\Psi = 30, 60$ and 90°, an elliptical motion is formed, whose plane rotates according to the value of Ψ.

4. Final remarks

This work elaborates on the physical effect of the magnetic field on the electron kinetics under AC/DC electric fields. More specifically, the main aim of the present effort is to provide the community an open-source MC code, extensively verified and benchmarked, that allows the study of the electron kinetics under AC/DC electric and DC magnetic fields crossed at arbitrary angles. This consists a significant update in comparison with the previous release of LoKI-MC [11], where only DC electric fields were considered. The most important modification is in the propagation of the electron position and velocity during the collision-free flights, which is taken into account with the analytical solutions of the

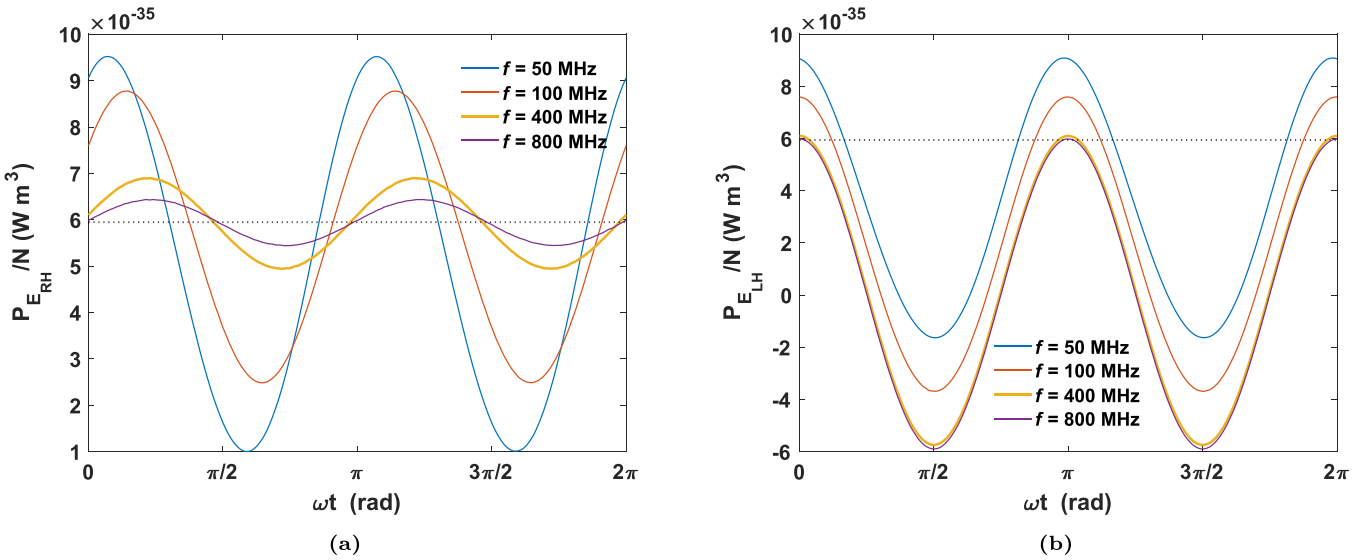


Figure 11. Reduced electric-field power absorbed due to the right-hand (a) and left-hand (b) circular fields, along the AC period, in the Reid-ramp model. The horizontal dotted line represents the power due to a DC electric field with $E_{\rm DC}/N = E_0/N/2 = 10/\sqrt{2}$ Td and null B.

Table 1. List of the AC frequencies f (in MHz), reduced angular frequencies ω/N (in 10^{-14} rad s^{-1} m^3) and $(\omega/N)/k_m^{\rm typ}$ (in 10^{-14} rad), in the Reid-ramp model, N_2 and Ar. The gas density is $N = 3.54 \times 10^{22}$ m^3. In the Reid-ramp model, $E_{\rm rms}/N = 10$ Td, while in N_2 and Ar, $E_{\rm rms}/N = 100$ Td.

Reid-ramp			N_2			Ar		
f	ω/N	$(\omega/N)/k_m^{\rm typ}$	f	ω/N	$(\omega/N)/k_m^{\rm typ}$	f	ω/N	$(\omega/N)/k_m^{\rm typ}$
50	0.887	0.52	400	7.10	0.85	200	3.55	0.25
100	1.775	1.04	800	14.20	1.70	400	7.10	0.49
200	3.55	2.08	1600	28.40	3.40	800	14.20	0.98
400	7.10	4.15	2400	42.60	5.10	1200	21.30	1.48
800	14.20	8.31	3200	56.80	6.80	1600	28.40	1.97

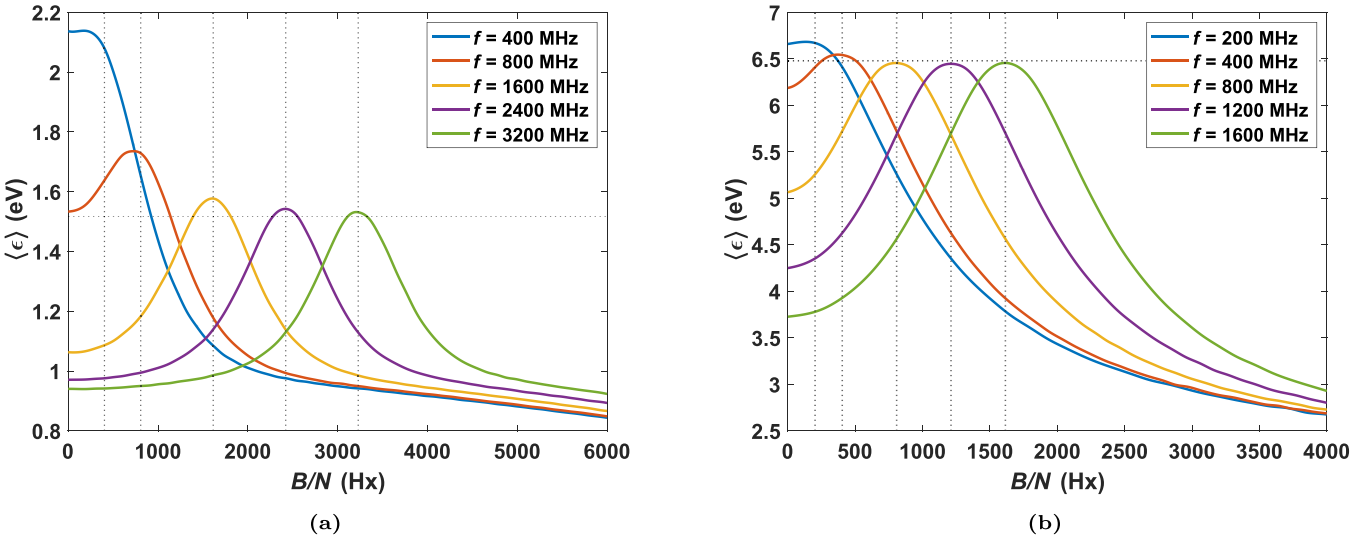


Figure 12. Electron mean energy $\langle\epsilon\rangle$, as a function of B/N, for different excitation frequencies f, in N_2 (a) and Ar (b). Vertical dotted lines indicate the values of B/N for which ECR occurs. Horizontal dotted lines represent the calculations using a DC electric field with $E_{\rm DC}/N = E_0/N/2 = 100/\sqrt{2}$ Td and null B.

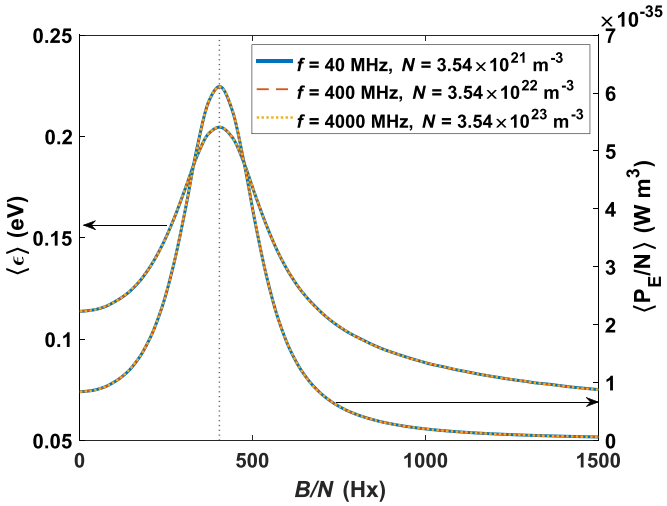


Figure 13. Electron mean energy $\langle\epsilon\rangle$ (left) and reduced electric-field power $\langle P_E/N\rangle$ (right), as a function of B/N, for three sets of f and N values, keeping ω/N constant, in the Reid-ramp model.

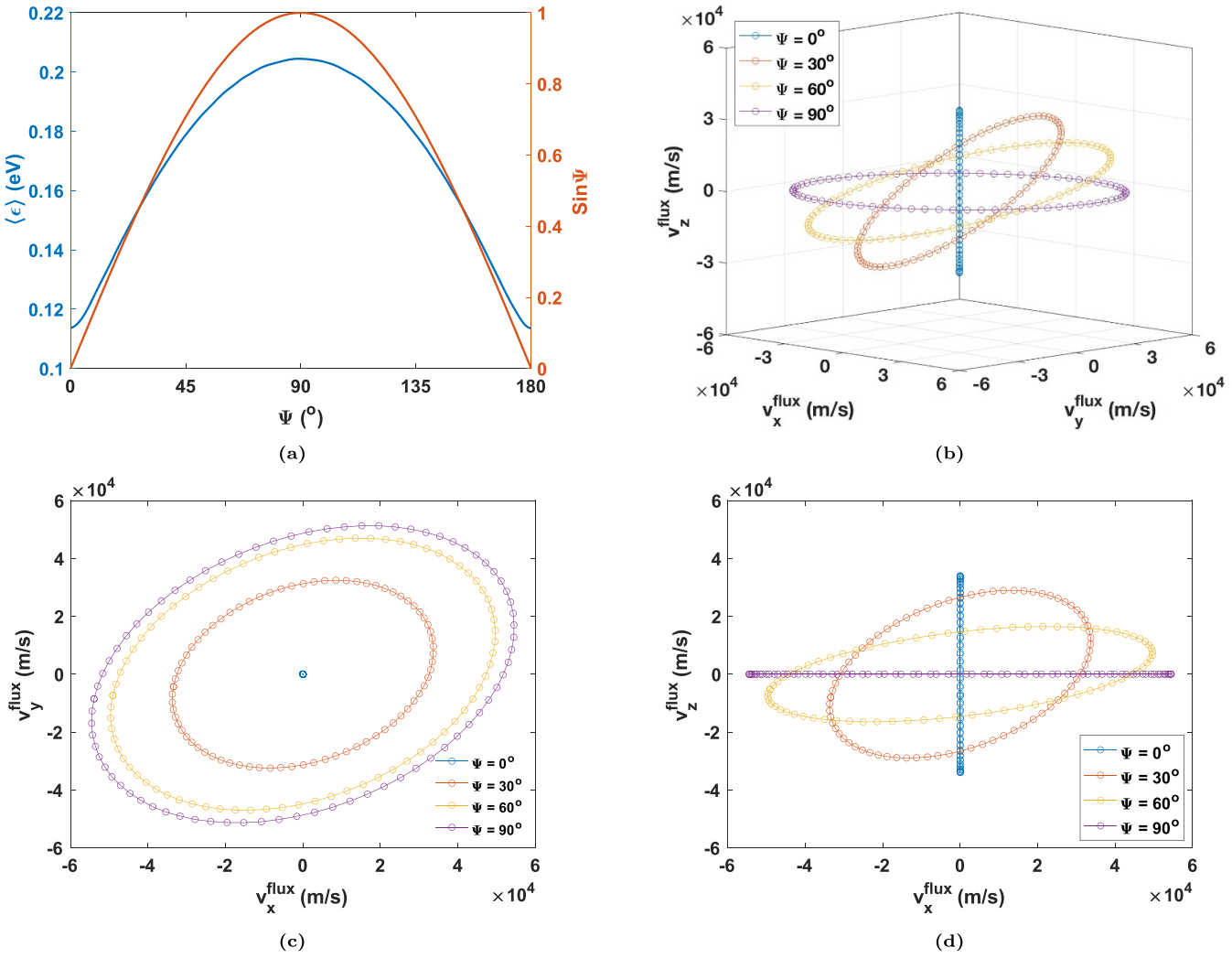


Figure 14. Time-averaged electron mean energy (a), as a function of Ψ. Electron drift velocity along an AC cycle, in 3D (b), xy plane (c) and xz plane (d), for $\Psi = 0, 30, 60$ and $90°$. The calculations are made in the Reid-ramp gas, with $f = 400$ MHz, $N = 3.54 \times 10^{22}$ m^3 and B/N such that $\Omega = \omega$ (resonance conditions).

equations of motion. Additionally, other improvements not directly related with the field configuration are presented here, such as the asynchronous electron advancement and a more correct renormalization of the electron number.

Another contribution of this work is the production of new benchmark calculations for electron kinetics solvers, in conditions of coexistent AC electric and DC magnetic fields. The calculations account for the temporal evolution along the AC cycle (figures 10 and 11), explore the effect of the crossing angle between the fields (figure 14), and highlight that the relevant parameters for the resonance curves in perpendicular configuration are E/N, B/N and ω/N (figure 13).

The role of the magnetic field in the electron acceleration is discussed, separating the cases with DC and AC electric fields. In DC electric fields, the oscillatory motion caused by the magnetic field decreases the efficiency of the electron acceleration, which reflects on the power absorbed by the electric field and on the electron mean energy. However, in Ar, for small transient regions of E/N and B/N, we find conditions where (i) for constant B/N, $\langle\epsilon\rangle$ decreases with increasing E/N and (ii) for constant E/N, $\langle\epsilon\rangle$ increases with increasing B/N. These counter-intuitive characteristics were first reported by Ness and Makabe [25] and are now confirmed by means of an independent MC simulation. The main source for this trend is related with the rapid increase of the elastic cross section from $\sim$0.25 up to 10 eV, followed by the steep appearance of strong inelastic losses after 11 eV.

In AC electric fields, when the magnetic field value is such that the electron cyclotron frequency Ω is similar to the angular frequency ω of the electric field, the synchronization of the cyclotron motion with the right-hand circular component of the electric field enhances electron acceleration, through the well-known ECR. However, for conditions where the mean collision frequency is much higher than the cyclotron frequency, the synchronization tends to breakdown and the magnetic field is detrimental for the electron acceleration, as in the DC electric field case.

The results in real gases demonstrate the robustness of the formulation implemented in LoKI-MC, allowing to study systems with interest for applications. At the same time, the similarities with the results obtained in model gases reinforce the great interest of studying fundamental physical phenomena in electron kinetics using these simplified models, whose calculations can be easily reproduced with different codes.

LoKI-MC proves to be an efficient tool, capable of delivering a statistically accurate solution for a given condition within minutes, even when run on a standard laptop. In general, the implementation of the magnetic field has little impact on the computational load, despite the increasing complexity of the equations of motion. However, when dealing with intermediate values of E/N in Ar, the magnetic field can result in noticeably longer computation times, reaching up to a few hours. This extended duration is due to an enhancement of null collisions, linked with a larger presence of electrons with energies near the Ramsauer minimum of the elastic cross section (cf figure 6). Additionally, the issue is exacerbated by the considerable number of simulated electron-neutral collisions required for an elastic gas as argon, where the energy exchange in each collision is weak. In the future, this concern might be partly mitigated with the implementation of optimized versions of the null collision technique (see e.g. [50]).

Future research efforts may include the study of the electron kinetics under electric and magnetic fields in gases with relevance in different applications, such as Xe for plasma propulsion, and Cl_2, SF_6 and CF_4 for plasma etching. Additionally, we could generalize the study to systems with AC magnetic fields [20, 23], but this is not straightforward since in that case the integration of the collision-free motion cannot be performed analytically. Finally, it would be interesting to investigate transient phenomena in combined electric and magnetic fields during the temporal relaxation of the electron swarm, which can unveil very exotic physics, such as transiently negative diffusion coefficients, as shown, e.g. in [51, 52]. LoKI-MC is not yet prepared for such configurations, but the extension should be straightforward.

Data availability statement

All data that support the findings of this study are included within the article (and any supplementary files).

Acknowledgments

This work was supported by the Portuguese FCT—Fundação para a Ciência e a Tecnologia, under Projects PTDC/FISPLA/1616/2021, MIT-EXPL/ACC/0031/2021, UIDB/50010/2020 and UIDP/50010/2020, and Grant PD/BD/150414/2019.

Appendix A. Integration of the collision-free motion

This section presents the analytical solutions of the Newton equation (2) for the propagation of the electron position ($\mathbf{r}$) and velocity ($\mathbf{v}$), from a time-instant t_0 up to $t_0 + t_c$, free of collisions. The general case ($\omega \neq 0$ & $B \neq 0$) is presented, as well as other particular conditions, such as $\omega = 0$, $B = 0$ and $\omega = \Omega = eB/m_e$ (electron cyclotron resonance). The following auxiliar variables are used:

$$\begin{cases} v_{x,t_0} = v_x(t_0), v_{y,t_0} = v_y(t_0), v_{z,t_0} = v_z(t_0) \\ x_{t_0} = x(t_0), y_{t_0} = y(t_0), z_{t_0} = z(t_0) \\ \phi = \omega t_0 \end{cases} . \tag{12}$$

A.1. General case ($\omega \neq 0$ & $B \neq 0$)

$$\begin{cases} v_x(t_0+t_c) = \frac{eE_{x,0}(\omega\sin(\phi)\cos(\Omega t_c)-\omega\sin(\omega t_c+\phi)+\Omega\cos(\phi)\sin(\Omega t_c))}{m(\omega^2-\Omega^2)} + v_{x,t_0}\cos(\Omega t_c) - v_{y,t_0}\sin(\Omega t_c) \\ v_y(t_0+t_c) = \frac{eE_{x,0}(\omega\sin(\phi)\sin(\Omega t_c)+\Omega\cos(\omega t_c+\phi)-\Omega\cos(\phi)\cos(\Omega t_c))}{m(\omega^2-\Omega^2)} + v_{x,t_0}\sin(\Omega t_c) + v_{y,t_0}\cos(\Omega t_c) \\ v_z(t_0+t_c) = \frac{eE_{z,0}(\sin(\phi)-\sin(\omega t_c+\phi))}{m\omega} + v_{z,t_0} \\ x(t_0+t_c) = \frac{eE_{x,0}(\sin(\phi)(\omega\sin(\Omega t_c)-\Omega\sin(\omega t_c))+\Omega\cos(\phi)(\cos(\omega t_c)-\cos(\Omega t_c)))}{m\Omega(\omega^2-\Omega^2)} + \frac{v_{x,t_0}\sin(\Omega t_c)}{\Omega} + \frac{v_{y,t_0}(\cos(\Omega t_c)-1)}{\Omega} + x_{t_0} \\ y(t_0+t_c) = \frac{eE_{x,0}\left(\sin(\phi)\left(\omega^2\cos(\Omega t_c)-\omega^2+\Omega^2\right)+\Omega(\omega\cos(\phi)\sin(\Omega t_c)-\Omega\sin(\omega t_c+\phi))\right)}{m\omega\Omega(\Omega^2-\omega^2)} + \frac{v_{x,t_0}(1-\cos(\Omega t_c))}{\Omega} + \frac{v_{y,t_0}\sin(\Omega t_c)}{\Omega} + y_{t_0} \\ z(t_0+t_c) = \frac{eE_{z,0}(\omega t_c\sin(\phi)+\cos(\omega t_c+\phi)-\cos(\phi))}{m\omega^2} + t_c v_{z,t_0} + z_{t_0}. \end{cases} \tag{13}$$

A.2. $\omega = 0$

$$\begin{cases} v_x(t_0+t_c) = -\frac{eE_{x,0}\sin(\Omega t_c)}{m\Omega} + v_{x,t_0}\cos(\Omega t_c) - v_{y,t_0}\sin(\Omega t_c) \\ v_y(t_0+t_c) = \frac{eE_{x,0}(\cos(\Omega t_c)-1)}{m\Omega} + v_{x,t_0}\sin(\Omega t_c) + v_{y,t_0}\cos(\Omega t_c) \\ v_z(t_0+t_c) = v_{z,t_0} - \frac{t_c eE_{z,0}}{m} \\ x(t_0+t_c) = \frac{eE_{x,0}(\cos(\Omega t_c)-1)}{m\Omega^2} + \frac{v_{x,t_0}\sin(\Omega t_c)}{\Omega} + \frac{v_{y,t_0}(\cos(\Omega t_c)-1)}{\Omega} + x_{t_0} \\ y(t_0+t_c) = \frac{eE_{x,0}(\sin(\Omega t_c)-\Omega t_c)}{m\Omega^2} + \frac{v_{x,t_0}(1-\cos(\Omega t_c))}{\Omega} + \frac{v_{y,t_0}\sin(\Omega t_c)}{\Omega} + y_{t_0} \\ z(t_0+t_c) = -\frac{t_c^2 eE_{z,0}}{2m} + t_c v_{z,t_0} + z_{t_0}. \end{cases} \tag{14}$$

A.3. $B = 0$

$$\begin{cases} v_x(t_0+t_c) = \frac{eE_{x,0}(\sin(\phi)-\sin(\omega t_c+\phi))}{m\omega} + v_{x,t_0} \\ v_y(t_0+t_c) = v_{y,t_0} \\ v_z(t_0+t_c) = \frac{eE_{z,0}(\sin(\phi)-\sin(\omega t_c+\phi))}{m\omega} + v_{z,t_0} \\ x(t_0+t_c) = \frac{eE_{x,0}(\omega t_c\sin(\phi)+\cos(\omega t_c+\phi)-\cos(\phi))}{m\omega^2} + t_c v_{x,t_0} + x_{t_0} \\ y(t_0+t_c) = t_c v_{y,t_0} + y_{t_0} \\ z(t_0+t_c) = \frac{eE_{z,0}(\omega t_c\sin(\phi)+\cos(\omega t_c+\phi)-\cos(\phi))}{m\omega^2} + t_c v_{z,t_0} + z_{t_0}. \end{cases} \tag{15}$$

A.4. $\omega = \Omega$

$$\begin{cases} v_x(t_0+t_c) = -\frac{eE_{x,0}(\Omega t_c\cos(\Omega t_c+\phi)+\cos(\phi)\sin(\Omega t_c))}{2m\Omega} + v_{x,t_0}\cos(\Omega t_c) - v_{y,t_0}\sin(\Omega t_c) \\ v_y(t_0+t_c) = -\frac{eE_{x,0}(\Omega t_c\sin(\phi)\cos(\Omega t_c)+\sin(\Omega t_c)(\Omega t_c\cos(\phi)-\sin(\phi)))}{2m\Omega} + v_{x,t_0}\sin(\Omega t_c) + v_{y,t_0}\cos(\Omega t_c) \\ v_z(t_0+t_c) = \frac{eE_{z,0}(\sin(\phi)-\sin(\Omega t_c+\phi))}{m\Omega} + v_{z,t_0} \\ x(t_0+t_c) = -\frac{eE_{x,0}(2\Omega t_c\sin(\Omega t_c+\phi)+\cos(\Omega t_c+\phi)-\cos(\phi-\Omega t_c))}{4m\Omega^2} + \frac{v_{x,t_0}\sin(\Omega t_c)}{\Omega} + \frac{v_{y,t_0}(\cos(\Omega t_c)-1)}{\Omega} + x_{t_0} \\ y(t_0+t_c) = \frac{eE_{x,0}(\Omega t_c\cos(\Omega t_c+\phi)-2\sin(\phi)(\cos(\Omega t_c)-1)-\cos(\phi)\sin(\Omega t_c))}{2m\Omega^2} + \frac{v_{x,t_0}(1-\cos(\Omega t_c))}{\Omega} + \frac{v_{y,t_0}\sin(\Omega t_c)}{\Omega} + y_{t_0} \\ z(t_0+t_c) = \frac{eE_{z,0}(\Omega t_c\sin(\phi)+\cos(\Omega t_c+\phi)-\cos(\phi))}{m\Omega^2} + t_c v_{z,t_0} + z_{t_0}. \end{cases} \tag{16}$$

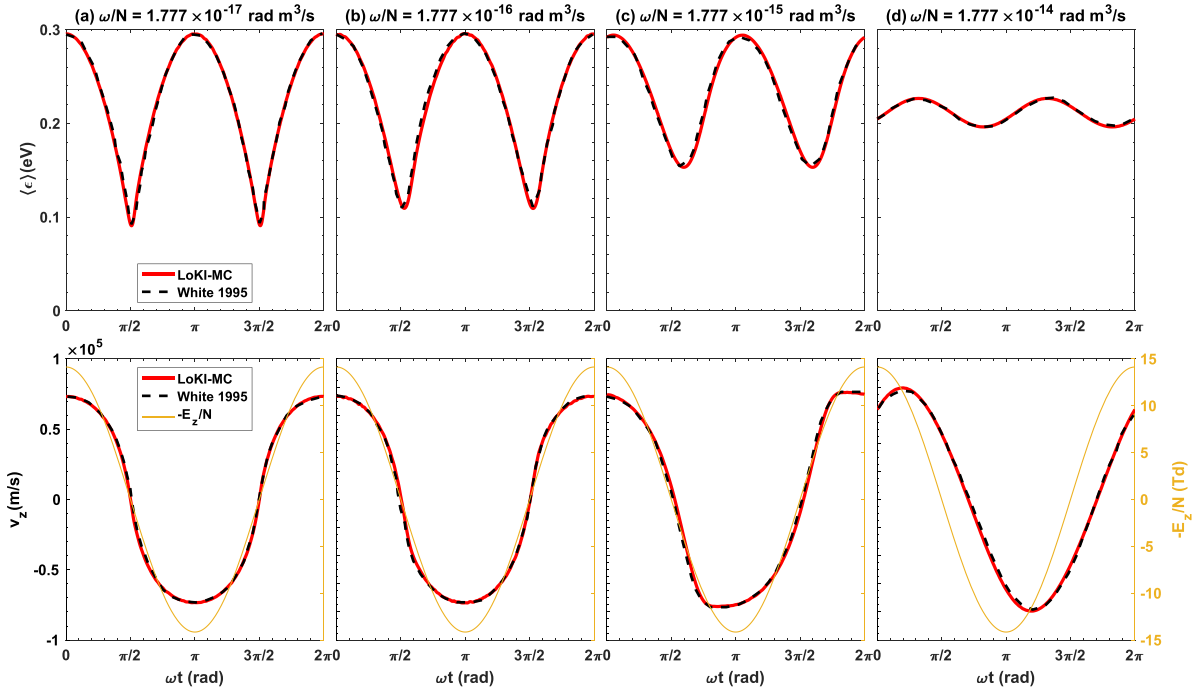


Figure 15. Comparison between the LoKI-MC calculations of the mean electron energy and drift velocity and the results from [34], for $B = 0$, different ω/N and using the Reid-ramp model. The results are shown as a function of the period phase ωt and the reduced electric field $-E_z/N$ is shown in yellow.

Appendix B. Benchmark with $B = 0$ and AC electric field

As additional info, and for completeness, we also present a comparison between LoKI-MC calculations and the results from [34], under an AC electric field and null magnetic field, using the Reid-ramp model. The reduced angular excitation frequency ω/N varies from 1.777×10^{-17} to 1.777×10^{-14} rad m^3 s^{-1}, the root-mean-squared reduced electric field is $E_{\mathrm{rms}}/N = 10$ Td and the angle between the z-axis and the electric field is $\Psi = 180°$. The mean electron energy $\langle\epsilon\rangle$ and the drift velocity v_z are shown in figure 15 as a function of the period phase ωt. The present calculations agree remarkably with the results from [34]. For an extended physical explanation of these results, the reader is referred to [34]. Here, we point out that, with increasing ω/N, (i) the fluctuations of the mean electron energy decrease significantly and (ii) a phase shift between the drift velocity and the electric field is evident. Note that LoKI-MC also passed with success a similar benchmark for the Lucas–Saelee gas model [35] (not shown here).

ORCID iDs

Tiago C Dias https://orcid.org/0000-0002-2179-1345
Carlos D Pintassilgo https://orcid.org/0000-0003-1527-2976
Vasco Guerra https://orcid.org/0000-0002-6878-6850

References

[1] Hagelaar G J M and Pitchford L C 2005 *Plasma Sources Sci. Technol.* **14** 722
[2] Dyatko N, Kochetov I, Napartovich A and Sukharev A 2015 EEDF: the software package for calculations of electron energy distribution function (available at: www.lxcat.net/software/EEDF/)
[3] Luque A 2014 BOLOS (available at: https://github.com/aluque/bolos)
[4] Tejero-del-Caz A, Guerra V, Gonçalves D, Lino da Silva M, Marques L, Pinhão N, Pintassilgo C D and Alves L L 2019 *Plasma Sources Sci. Technol.* **28** 043001
[5] Tejero-del-Caz A, Guerra V, Pinhão N, Pintassilgo C D and Alves L L 2021 *Plasma Sources Sci. Technol.* **30** 065008
[6] Stephens J 2018 *J. Phys. D: Appl. Phys.* **51** 125203
[7] Rabie M and Franck C M 2016 *Comput. Phys. Commun.* **203** 268
[8] Biagi S 1999 *Nucl. Instrum. Methods Phys. Res.* A **421** 234
[9] Renda M, Ciubotaru D and Banu C 2021 *Comput. Phys. Commun.* **267** 108057
[10] Teunissen J, Martinez A and Sun A 2015 Particle_swarm (available at: https://gitlab.com/MD-CWI-NL/particle_swarm)
[11] Dias T C, Tejero-del-Caz A, Alves L L and Guerra V 2023 *Comput. Phys. Commun.* **282** 108554
[12] Phelps A V and Pitchford L C 1985 *Phys. Rev.* A **31** 2932
[13] White R D, Robson R E, Schmidt B and Morrison M A 2003 *J. Phys. D: Appl. Phys.* **36** 3125
[14] Reid I 1979 *Aust. J. Phys.* **32** 231
[15] Budde M, Dias T C, Vialetto L, Pinhão N, Guerra V and Silva T 2023 *J. Phys. D: Appl. Phys.* **56** 255201
[16] Shon C and Lee J 2002 *Appl. Surf. Sci.* **192** 258

[17] Keidar M, Zhuang T, Shashurin A, Teel G, Chiu D, Lukas J, Haque S and Brieda L 2014 *Plasma Phys. Control. Fusion* **57** 014005
[18] Mrózek K, Dytrych T, Moliš P, Dániel V and Obrusník A 2021 *Plasma Sources Sci. Technol.* **30** 125007
[19] Makabe T and Petrovic Z 2015 *Plasma Electronics* 2nd edn (CRC Press)
[20] Petrović Z, Raspopović Z, Dujko S and Makabe T 2002 *Appl. Surf. Sci.* **192** 1
[21] White R, Ness K and Robson R 2002 *Appl. Surf. Sci.* **192** 26
[22] Dujko S, Raspopović Z M and Petrović Z L 2005 *J. Phys. D: Appl. Phys.* **38** 2952
[23] Dujko S, Bošnjaković D, White R D and Petrović Z L 2015 *Plasma Sources Sci. Technol.* **24** 054006
[24] Nakamura S, Ventzek P L G and Kitamori K 1999 *J. Appl. Phys.* **85** 2534
[25] Ness K and Makabe T 2000 *Phys. Rev.* E **62** 4083
[26] Raspopović Z M, Dujko S, Makabe T and Petrović Z L 2005 *Plasma Sources Sci. Technol.* **14** 293
[27] White R, Robson R and Ness K 1999 *IEEE Trans. Plasma Sci.* **27** 1249
[28] White R D, Ness K F and Robson R E 1999 *J. Phys. D: Appl. Phys.* **32** 1842
[29] Dujko S, White R D, Petrović Z L and Robson R E 2011 *Plasma Sources Sci. Technol.* **20** 024013
[30] Raju G R and Gurumurthy G R 1978 *Int. J. Electron.* **44** 355
[31] Raju G and Dincer M 1990 *IEEE Trans. Plasma Sci.* **18** 819
[32] Dincer M S, Tezcan S S and Duzkaya H 2018 *AIP Adv.* **8** 095026
[33] Lucas J and Saelee H T 1975 *J. Phys. D: Appl. Phys.* **8** 640
[34] White R D, Robson R E and Ness K F 1995 *Aust. J. Phys.* **48** 925
[35] White R D, Robson R E and Ness K F 1999 *Phys. Rev.* E **69** 7457
[36] White R D, Brennan M J and Ness K F 1997 *J. Phys. D: Appl. Phys.* **30** 810
[37] Raspopovic Z M, Sakadzic S, Bzenic S A and Petrovic Z L 1999 *IEEE Trans. Plasma Sci.* **27** 1241
[38] Dujko S, White R D, Petrović Z L and Robson R E 2010 *Phys. Rev.* E **81** 046403
[39] Skullerud H R 1968 *J. Phys. D: Appl. Phys.* **1** 1567
[40] Longo S 2000 *Plasma Sources Sci. Technol.* **9** 468
[41] White R D, Ness K F, Robson R E and Li B 1999 *Phys. Rev.* E **60** 2231
[42] Mirić J, Bošnjaković D, Simonović I, Petrović Z L and Dujko S 2016 *Plasma Sources Sci. Technol.* **25** 065010
[43] Longo S 2006 *Plasma Sources Sci. Technol.* **15** S181
[44] Hockney R W and Eastwood J 1988 *Computer Simulation Using Particles* 1st edn (CRC Press)
[45] Ness K F and Robson R E 1986 *Phys. Rev.* A **34** 2185
[46] N_2 and Ar on IST-Lisbon data (available at: www.lxcat.net)
[47] Heylen A E D and Dargan C L 1973 *Int. J. Electron.* **35** 433
[48] Loureiro J and Amorim J 2016 *Kinetics and Spectroscopy of Low Temperature Plasmas* (Wiley)
[49] Asmussen J 1989 *J. Vac. Sci. Technol.* A **7** 883
[50] Brennan M 1991 *IEEE Trans. Plasma Sci.* **19** 256
[51] White R D, Dujko S, Ness K F, Robson R E, Raspopović Z and Petrović Z L 2008 *J. Phys. D: Appl. Phys* **41** 025206
[52] White R D, Dujko S, Robson R E, Petrović Z L and McEachran R P 2010 *Plasma Sources Sci. Technol.* **19** 034001